Ocean Systems Engineering, *Vol. 14, No. 2 (2024) 115-139*
https://doi.org/10.12989/ose.2024.14.2.115

Dynamic analysis of floating bridges under combined earthquakes and waves

Ikjae Lee[1], Moohyun Kim[*1], Jihun Song[2] and Seungjun Kim[2]

[1]*Department of Ocean Engineering, Texas A&M University, College Station, TX, 77840, USA*
[2]*School of Civil, Environmental and Architectural Engineering, Korea University, Seoul 02841, Republic of Korea*

(Received March 22, 2024, Revised May 20, 2024, Accepted May 25, 2024)

Abstract. In this study, numerical study of a long, straight, side-anchored floating bridge with discrete pontoons subjected to combined earthquakes and waves is conducted. Ground motions with magnitude corresponding to 200 YRP (years return period) earthquake in South Korea are generated based on the spectral matching method from a past earthquake record in California. Several sensitivity studies are carried out for bridge end condition, for different site classes (hard rock S1 and soft and deep soil S5), and for three different excitations (earthquake only, wave only, and earthquake-wave combined). Bridge and pontoon motions, bending moments along the bridge, and mooring tensions are systematically examined through coupled time-domain simulations by commercial program OrcaFlex. The numerical results show that the impact of earthquakes on floating bridges is still of importance especially for soft soil although ground motions are less directly applied to the structure than fixed bridges.

Keywords: bending moment; discrete pontoon; dynamic response; earthquake; floating bridge; mooring tension

1. Introduction

Floating bridges offer a promising solution for spanning long distances in deep waters, particularly in cases where traditional bottom-fixed bridges prove less economically viable (Jang *et al.* 2020a). The successful construction/operation of several floating bridges worldwide has proven the feasibility of this technology. For instance, countries like the USA, Norway, Canada, and Guyana have embraced floating bridge construction, enabling the transportation of people and automobiles. In general, there are three main designs for floating bridges: the discrete pontoon type, continuous pontoon type, and floating tower and cable-supported type. In addition, the design can also be classified into curved and straight bridges. The present study focuses on the straight discrete-pontoon floating bridge designed for Bjørnafjord on West Coast of Norway (See Fig. 1).

The main difficulty of the floating bridge design lies in its complex environmental loads due to severe winds, currents, waves, and earthquakes. The dynamic analyses of various types of floating bridges subjected to complex environments were carried out experimentally and numerically by several researchers. Yadi *et al*. (2018) performed 1:160 scaled multi-directional shake table tests for

*Corresponding author, Professor, E-mail: m-kim3@tamu.edu

 ISSN: 2093-6702 (Print), 2093-677X (Online)

Fig. 1 Bjørnafjord crossing on West Coast of Norway (Multiconsult 2017)

a floating bridge under earthquake excitation during construction based on Kobe earthquake record. Yan *et al.* (2023, 2024a) conducted 1:100 scale experiment to investigate dynamic behaviors of an end-anchored floating bridge under combined earthquakes and waves, earthquakes in still water, and pure waves without earthquakes. The same research group also carried out time-domain numerical simulations of a floating bridge under joint actions of earthquake and wave (Yan *et al*. 2024b).

Xiang *et al.* (2023) conducted a scaled experimental study at a 1:70 ratio on a floating bridge equipped with a mooring system, with the aim of measuring the structural responses induced by waves. Jin *et al*. (2020) investigated the dynamic behavior of a curved floating bridge with discrete pontoons using coupled time-domain dynamic analysis. Cheng *et al*. (2018a, b, 2019, 2020) explored the impact of inhomogeneous wave on the hydrodynamic responses of a side-anchored floating curved bridge. Won *et al.* (2020) and Jang *et al*. (2020b) explored the short-term fatigue and failure of floating bridge tethers subjected to severe wave conditions using hydrodynamics-based numerical simulations. Dai *et al*. (2020) investigated inhomogeneous wave load effects on a long, straight, and side-anchored floating pontoon bridge, which is also employed in the present paper for combined waves and earthquakes. Viuff *et al*. (2020a, 2023) studied numerical analysis methodologies for a long side-anchored floating curved bridge with a stay-cable tower, specifically conceptualized for Bjørnafjord. They investigated its uncertainty with a model test. The same research group also evaluated the uncertainty in various numerical models of floating bridges to enhance experimental methodologies and numerical analyses (Viuff *et al*. 2020b, Rodrigues *et al*. 2022). Jin *et al*. (2024) further investigated the feasibility of tuned mass damper for the vibration control of the curved floating bridge under wind and wave excitations.

For numerical modeling of the floating bridge, a reliable commercial software OrcaFlex (Orcina, 2024) has been employed in many researches. The program enables users to easily superpose multiple different types of excitations and/or motions.

The paper consists of 5 sections. In Section 2, the general description of target structure and its OrcaFlex modeling are given. In Section 3, the generation of target earthquake spectra and ground motions, and the implementation of the generated ground motions in the program OrcaFlex are detailed. In Section 4, sensitivity studies due to site classes (hard rock or soft and deep soil), bridge end boundary conditions (with or without earthquake), and earthquakes with or without waves are presented. Finally, the paper is concluded with several remarks in Section 5.

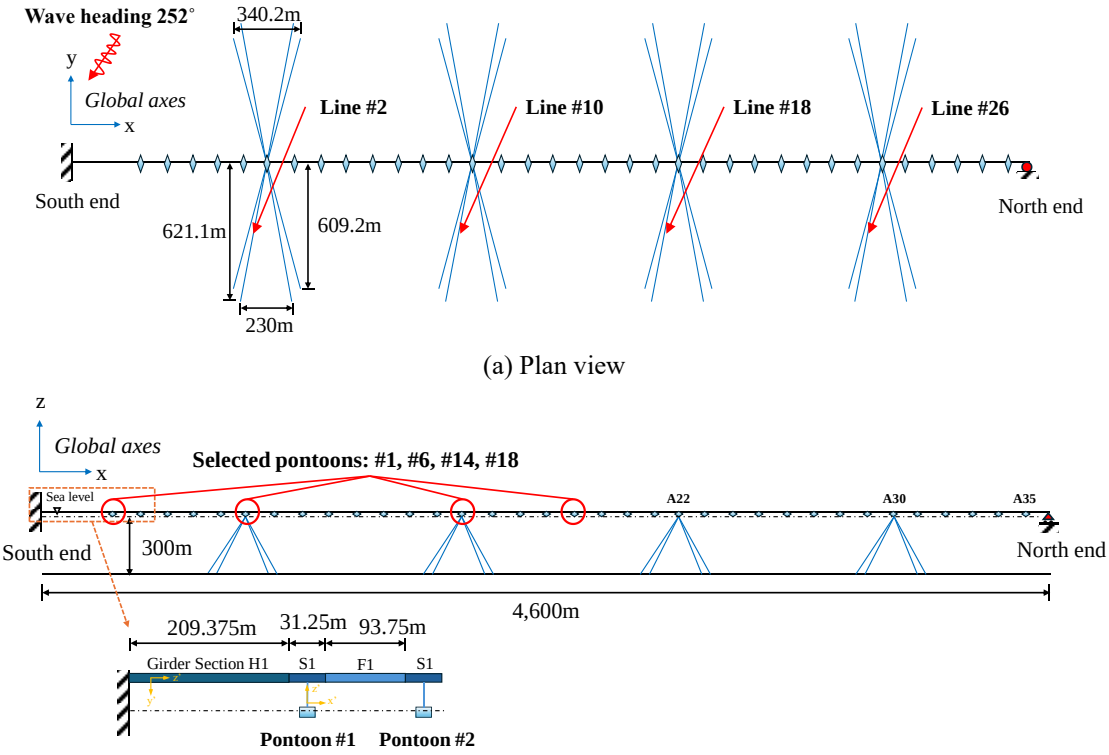

(a) Plan view

(b) Side view

Fig. 2 Idealized straight floating bridge: (a) plan and (b) side view

2. Target floating bridge and its modeling

2.1 System particulars

The original model documented by Multiconsult (2017) incorporates the stay-cable tower, seabed terrain characteristics of the target site, and more intricate components for the design of the floating bridge at Bjørnafjord. In this study, the straight and side-anchored floating pontoon bridge model reproduced the numerical model proposed by Dai *et al*. (2020), offering an idealized representation that efficiently captures the behavioral traits of the original design. As depicted in Fig. 2, the stay-cable tower was simplified to a line element with equivalent section stiffness, and each pontoon, girder, and column was arranged at the same level. The total length of the bridge spans 4,600 meters, with a separation distance of 125 meters between pontoons. The columns, standing at 14.5 meters in height, are rigidly connected to both the upper surface of the pontoons and the girders. Mooring lines, as depicted in Fig. 2(a), are fastened to four specific pontoons spaced 1,000 meters apart, each comprising eight strands forming a single cluster. Fig. 3 illustrates the pontoon model for the diffraction and radiation analysis of individual pontoons. The waterplane area shape comprises segments of five circles arranged as shown in Fig. 3. The center of flotation aligns with the center of gravity. The spacing between the pontoons ensures that hydrodynamic interactions between adjacent pontoons are insignificantly considered.

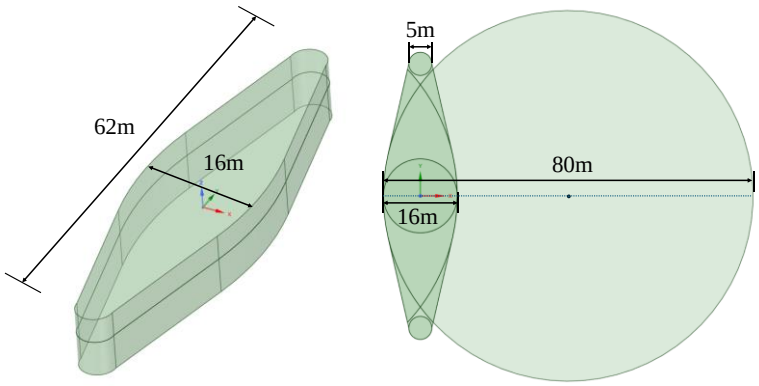

Fig. 3 Dimensional specifications of the pontoon

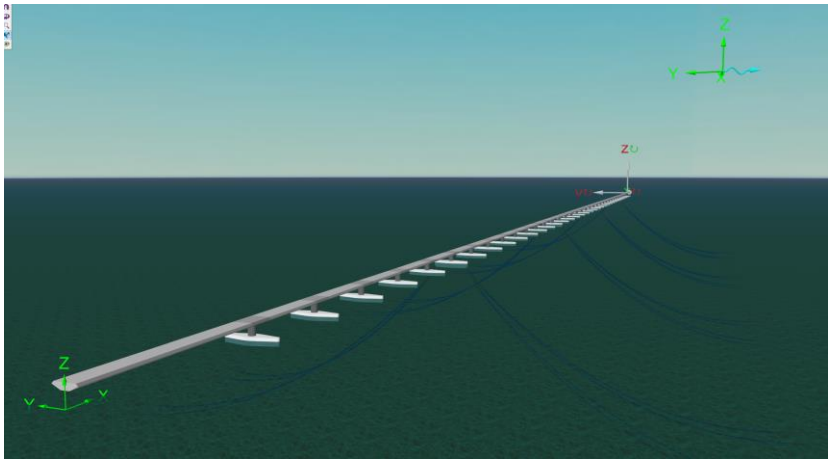

Fig. 4 Straight floating ponton bridge model in OrcaFlex

2.2 Numerical modeling in OrcaFlex

The numerical model of the floating pontoon bridge was established using OrcaFlex, as illustrated in Fig. 4. In OrcaFlex, the local z-axis of the line element is fixed to the direction of length, with the default configuration being the shear flexible beam element. The beam orientation for each line element was aligned as shown in Fig. 2(b). To prevent overlapping connections, Girder S1 was arranged with free-end connections at a height of 18 meters, while Girder F1 served as a link between Girder S1. All connections were assumed to be rigid. A fixed boundary condition was implemented at the South end, whereas only axial elongation and transverse rotation were permitted at the North end. The equivalent section properties and specifications for modeling the structural components are organized in Tables 1-3. Pretension was applied to the mooring lines, with 1,400 kN for the outer clusters and 1,522 kN for the inner clusters. The modified length of the mooring lines governs the change in total stiffness and natural periods of the system.

Table 1 Equivalent section properties of structural components

Section	Mass (te/m)	Axial rigidity EA (kN)	Bending rigidity $EI_{x'}$ (kN·m^4)	Bending rigidity $EI_{y'}$ (kN·m^4)	Torsional rigidity $GI_{z'}$ (kN·m^4)
Girder H1	17.53	289.8e6	602.7e6	22.52e9	467.7e6
Girder S1	19.78	346.5e6	852.6e6	24.47e9	636.5e6
Girder F1	16.04	245.7e6	674.1e6	18.87e9	536.3e6
Column	9.18	321.3e6	2.717e9	2.026e9	1.205e9

Table 2 Mooring line specifications

Segment	Nominal Diameter (mm)	Length (m)	Mass (te/m)	Axial stiffness (kN)
Top Chain	147	50	0.4735	1.95e6
Wire	124	600	0.0632	950e3
Bottom Chain	147	50	0.4735	1.95e6

Table 3 Pontoon properties.

Type	Freeboard (m)	Draft (m)	Mass (te)	Displaced Volume (m^3)	Radius of gyration		
					$r_{x'}$ (m)	$r_{y'}$ (m)	$r_{z'}$ (m)
Unmoored	3.5	5	850	3315.39	16.1	5.2	16.3
Moored	3.5	8.5	1452	5271.20	17.0	6.5	17.0

2.3 Modal analysis results: mode shapes and modal periods

The natural periods of the replicated floating bridge were tabulated in Table 4 and compared to the reference models. The fundamental period was observed in the lateral bending mode at 32.2 seconds. However, due to the boundary condition at the North end allowing elongation and transverse rotation, torsional bending mode was observed at lower periods. Furthermore, because of the numerous segments of mooring lines, vibration modes for the mooring lines themselves were observed at higher modes and were interspersed among the bending modes of the girder. Despite the algorithmic differences in static analysis between SIMO-RIFLEX and OrcaFlex, the maximum error of around 8% indicates that the replicated model exhibits good agreement in capturing the characteristics of the referenced floating bridges (Viuff *et al*. 2020a). Mode shapes of the reproduced floating bridge model is organized in Fig. 5 to give a clear representation of vibration characteristics. In the subsequent sections, seismic loads were applied to the replicated floating bridge to evaluate dynamic and structural responses under various loading conditions.

3. Generation and numerical implementation of ground motions

3.1 Matched spectra for South Korea and ground motions

The spectral matching method is widely adopted in order to generate design response spectra based on the location and site classes. The response of floating bridges in softer soil would be a

Table 4 Natural periods of floating bridge

Mode	Dominant axis	Natural period (Dai *et al.* 2020)	Natural period (Multiconsult 2017)	Natural period (Reproduced)
1st	y-axis (transverse)	34.1s	34.4s	32.2s
2nd	y-axis	31.2s	30.9s	31.5s
3rd	y-axis	30.3s	29.0s	28.5s
4th	y-axis	20.1s	21.2s	20.3s
5th	y-axis	15.5s	15.1s	17.0s
41st	y-axis	7.2s	7.4s	7.6s
44th	z-axis (vertical)	7.0s	7.0s	6.9s
46th	rx-axis (torsional)	6.7s	6.8s	6.7s
47th	rx-axis	6.6s	6.4s	6.4s
48th	rx-axis	6.6s	6.3s	6.3s

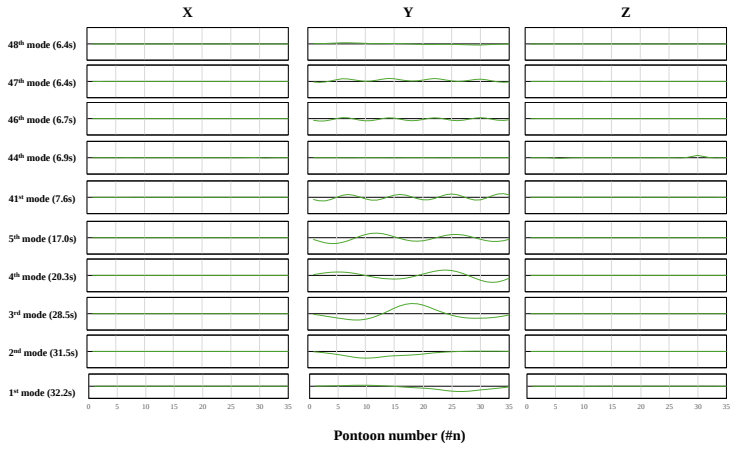

(a) Translational mode shapes

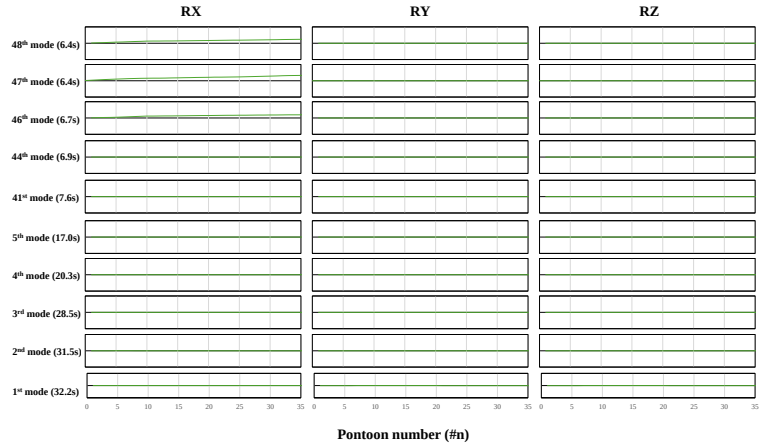

(b) Rotational mode shapes

Fig. 5 Modal analysis results of reproduced floating bridge

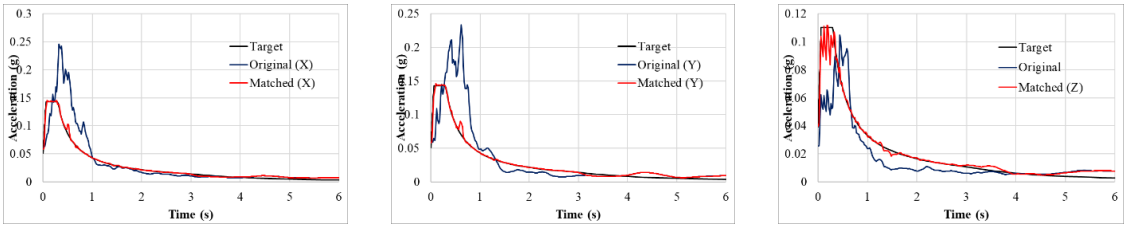

(a) Horizontal X-direction (b) Horizontal Y-direction (c) Vertical Z-direction

Fig. 6 X-Y-Z earthquake acceleration spectra for hard rock (S1)

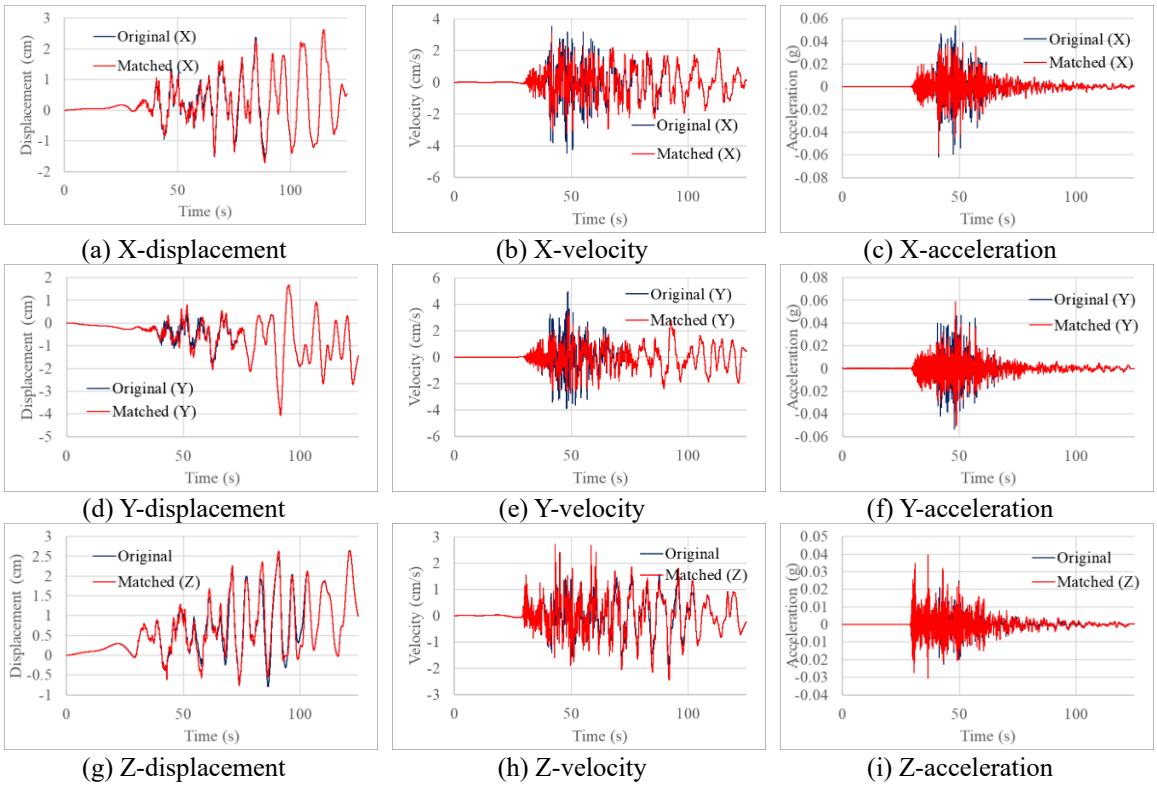

(a) X-displacement (b) X-velocity (c) X-acceleration

(d) Y-displacement (e) Y-velocity (f) Y-acceleration

(g) Z-displacement (h) Z-velocity (i) Z-acceleration

Fig. 7 Seismic ground motions for hard rock (S1): displacement, velocity, accelerations)

concern due to wider range of ground excitation frequencies. The interactions due to combined earthquakes and waves are also likely to be significant.

The multi-directional (X, Y, and Z) ground acceleration time histories are available in USGS NSMP (National Strong-Motion Project) Earthquake Data Sets (https://escweb.wr.usgs.gov/nsmp-data/nsmn_eqdata.html). We selected an earthquake record of moment magnitude 6.8 occurred in California area. The target response spectra for South Korea with magnitude corresponding to 200 YRP (years return period) for two different site classes: hard rock (S1) and deep and soft ground

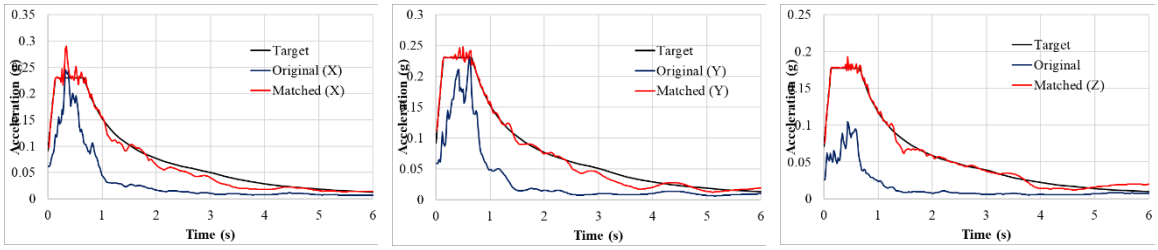

(a) Horizontal X-direction (b) Horizontal Y-direction (c) Vertical Z-direction

Fig. 8 Acceleration spectra for deep and soft ground (S5)

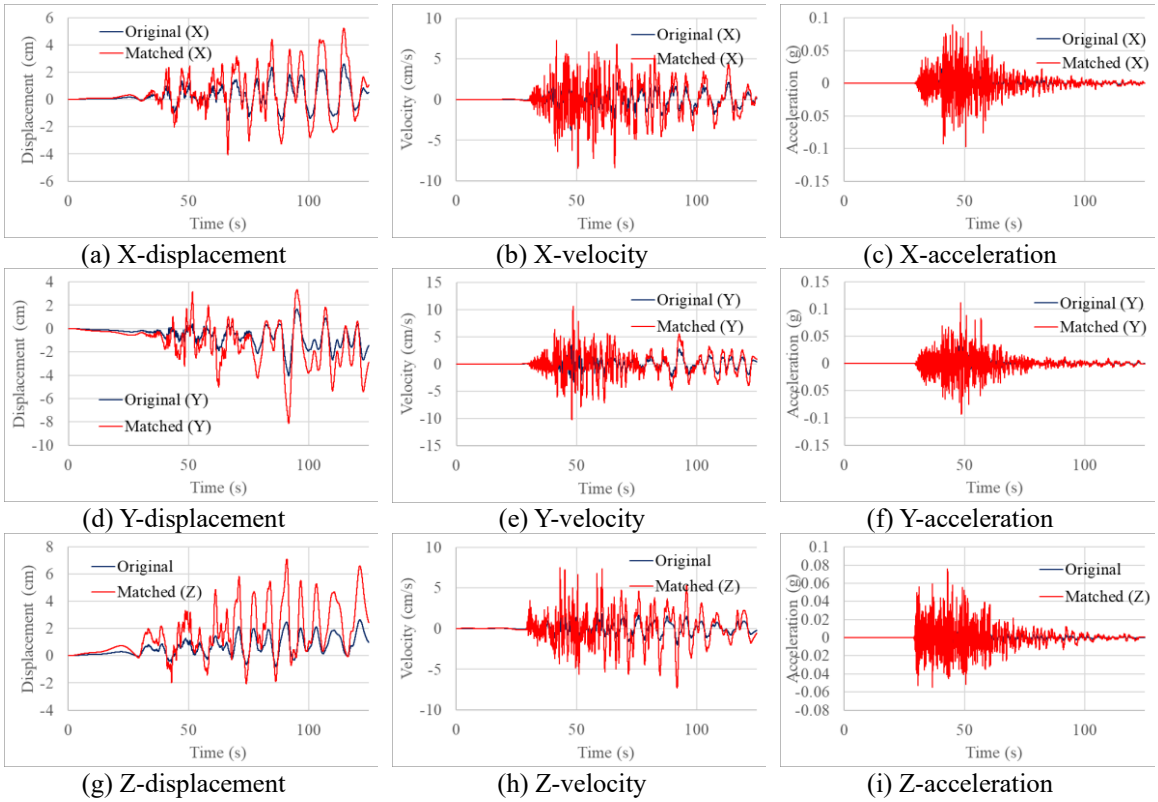

(a) X-displacement (b) X-velocity (c) X-acceleration

(d) Y-displacement (e) Y-velocity (f) Y-acceleration

(g) Z-displacement (h) Z-velocity (i) Z-acceleration

Fig. 9 Seismic ground motions for deep and soft ground (S5): displacement, velocity, accelerations

(S5) were generated. The design spectra for X, Y, and Z directions for S1 are illustrated in Figs. 6(a)-6(c) and the corresponding ground motions (displacement, velocity, acceleration) in Figs. 7(a)-7(i). This matching method utilizes the wavelet algorithm suggested by Al Atik and Abrahamson (2010). It should be noted that the vertical spectrum accounts for 77% of the horizontal spectrum. Likewise, in Figs. 8 and 9, the matched spectra and ground motions for S5 are given. It is seen that the earthquake displacements in soft soil are generally larger than those of hard rock.

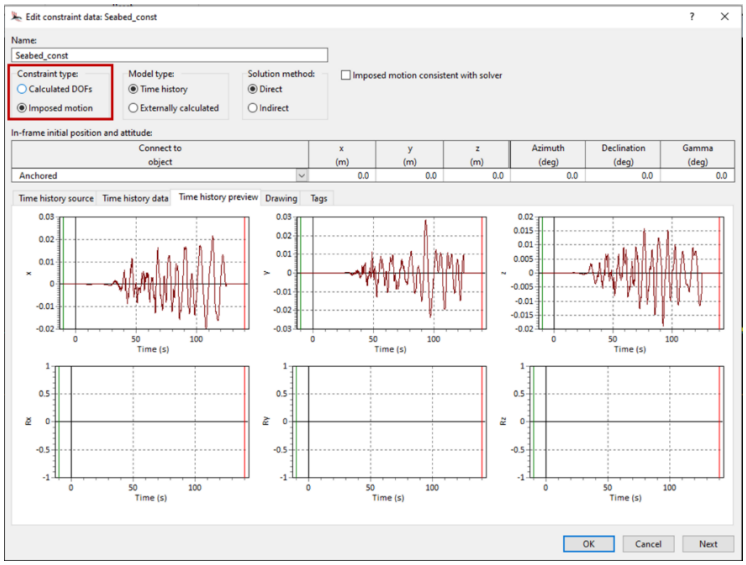

Fig. 10 Edit window of "Constraint" object

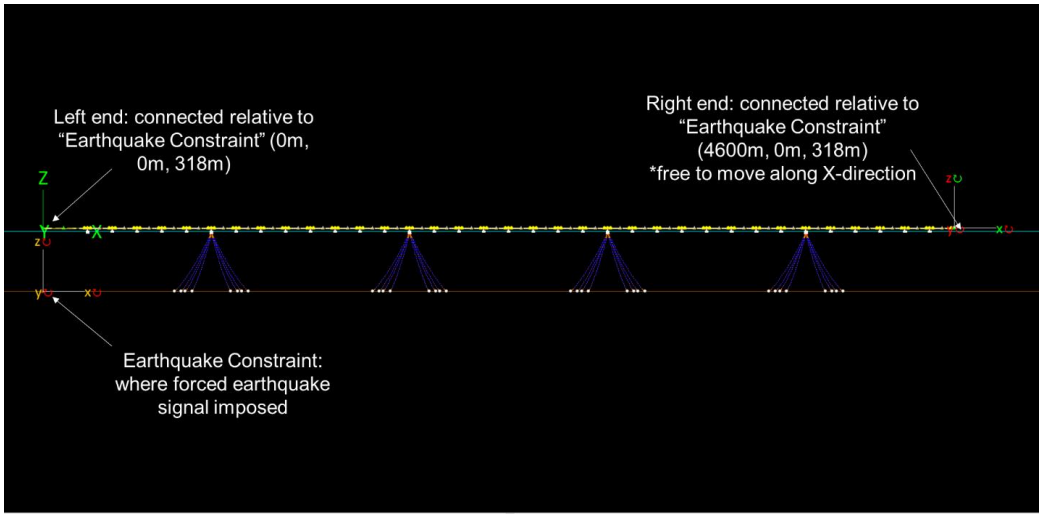

Fig. 11 An overview of the floating bridge configuration for earthquake simulation

3.2 Methodology to impose seismic motions in OrcaFlex

In order to realize the generated seismic motions in the program OrcaFlex, one has to input externally generated time-series data into the program. There are two objects in OrcaFlex that can receive the externally generated time-series motion data: (a) Vessel and (b) Constraint. In this study, we adopted the second object "Constraint" to impose the forced seismic motions. Considering that the speed of seismic waves is of order O(km/sec), seismic motions at all anchor locations and bridge ends are fully correlated such that their phases have no difference.

As an example, editing window of the "Constraint" object for the seabed seismic motion is shown in Fig. 10. As highlighted by red, "Imposed motion" is selected, in which one may either receive the externally generated 6-DOFs time-series data or manually generate it. By connecting one ends of all the mooring legs to this object, the forced oscillations can be transferred across the entire system. In addition, since seismic motions cover large area encompassing the entire bridge, we placed the simultaneous seismic motions to both ends of the bridge as well. Indeed, the right end of the bridge is allowed to move freely along x-direction. Therefore, the seismic motion is applied to only Y- and Z-directions at this location. An overview of the system configuration for earthquake simulation is shown in Fig. 11.

The bridge is secured by mooring lines on the seabed while both ends are connected to the land, thereby the bridge may be under two different soil conditions. As mentioned earlier, we restrict the scope of present study to simpler scenarios, where the earthquakes from land and seabed are exactly the same in phase and magnitude by assuming the same site classes.

4. Numerical results and analysis/discussion

The design concept and the idealized models are shown in Fig. 2. The details of the bridge girder, column, pontoon and mooring line properties are given in (Dai *et al*. 2023). For simplicity, the inclined tension cables near the left end above the bridge were not modeled in the present study.

4.1 Driving factors of seismic responses in S5 (deep soft) soil

As shown in Fig. 2, the mooring lines are based on a standard composition for a taut to semi taut system that ensure minimal bridge offset (Multiconsult 2017). However, the mooring system incorporates catenary-like arc shape which is maintained by the weight of the mooring lines. The water depth is 300m for this study. Accordingly, the seismic motions at anchors do not directly affect the structural response of the bridge except at both ends. Instead, the ground motions are transferred to the bridge through mooring lines. In this regard, we investigate the following scenarios

- Case-1: Seismic motions at anchors
- Case-2: Seismic motions at anchors + two bridge ends: left end for XYZ-directions; right end for YZ-directions (free for X-direction)

so that we may better understand which is more influential factor that govern the bridge motions and structural responses.

We carried out earthquake simulations for 6 minutes and checked typical statistical values across the girders of the bridge. The soil condition is assumed deep and soft (S5). In Figs. 12(a) and 12(b), the vertical and horizontal bending moment diagrams are generated, respectively, and compared between two scenarios. Similarly, the statistical values of girder for 3-DOF (X, Y, and Z) dynamic displacements are present in Figs. 12(c), 12(d), and 12(e).

In case of vertical bending moment (Fig. 12(a)), the distribution of standard deviation indicates that case 2 provides more dynamic effects on girders than case 1 i.e., when both ends are fixed, the seabed motions are hardly transferred to girders through mooring lines. However, the bending moment due to static equilibrium dominates over the dynamic response as shown in the distribution of maximum values. Moreover, since the rotational DOF for Z-axis (yaw) is free at the right end of the bridge according to the idealized model in Ref. (Dai *et al*. 2020), thus the corresponding bending moment at this location becomes zero. On the other hand, Fig. 12(b) shows that the standard

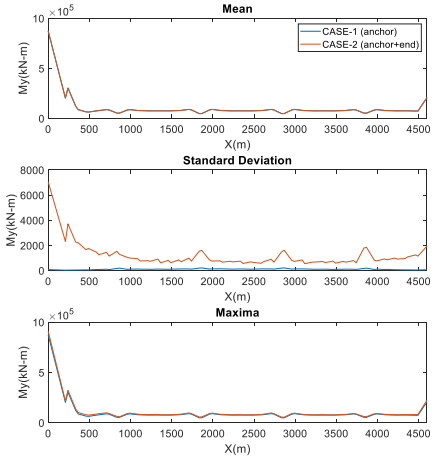

(a) Vertical bending moment

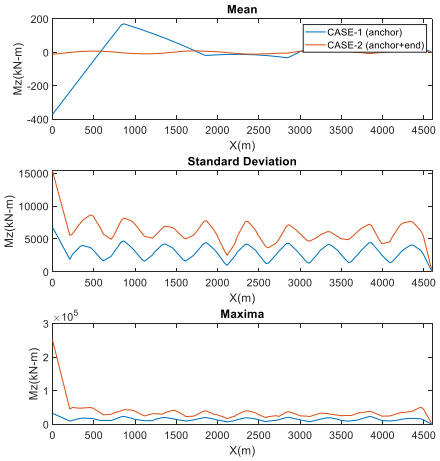

(b) Horizontal bending moment

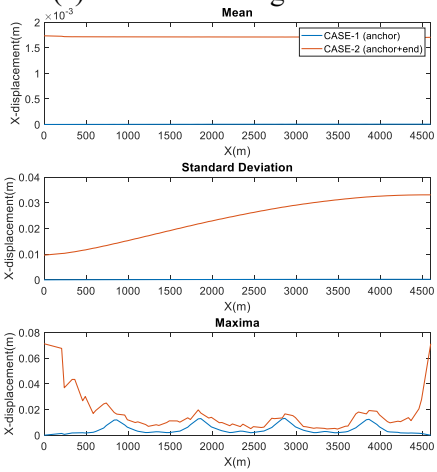

(c) girder X-displacement

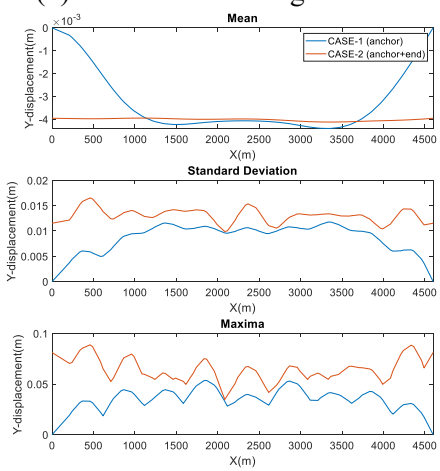

(d) girder Y-displacement

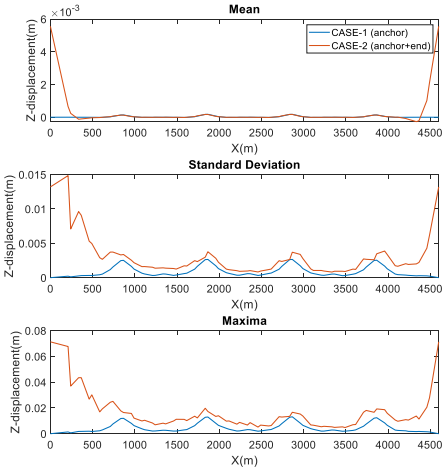

(e) girder Z-displacement

Fig. 12 Statistical values across bridge

deviation of the Case-1 is about half of the Case-2 and there is larger discrepancy in the maxima at the left end of the bridge.

Fig. 12(c) (X-displacement) shows that the standard deviation of the Case-2 increases as it goes from left to right. This is because the right end for this DOF is allowed to move freely. In addition, one can observe 4 minor peaks in the maxima in Case 1. At these points, pontoons are moored by the respective mooring groups. It indicates that the girder responses around these points are directly driven by seismic motions transferred via mooring lines. In Case 2, the overall motion responses are the largest at the two bridge ends since they are also directly driven by the earthquake.

4.2 Earthquake only simulation (S1 vs S5): Seismic motions at anchors + two bridge ends

In this section, the cases of two different soil conditions are compared. The earthquake simulations were performed for hard rock (S1) and deep and soft ground (S5) for 6 minutes. To

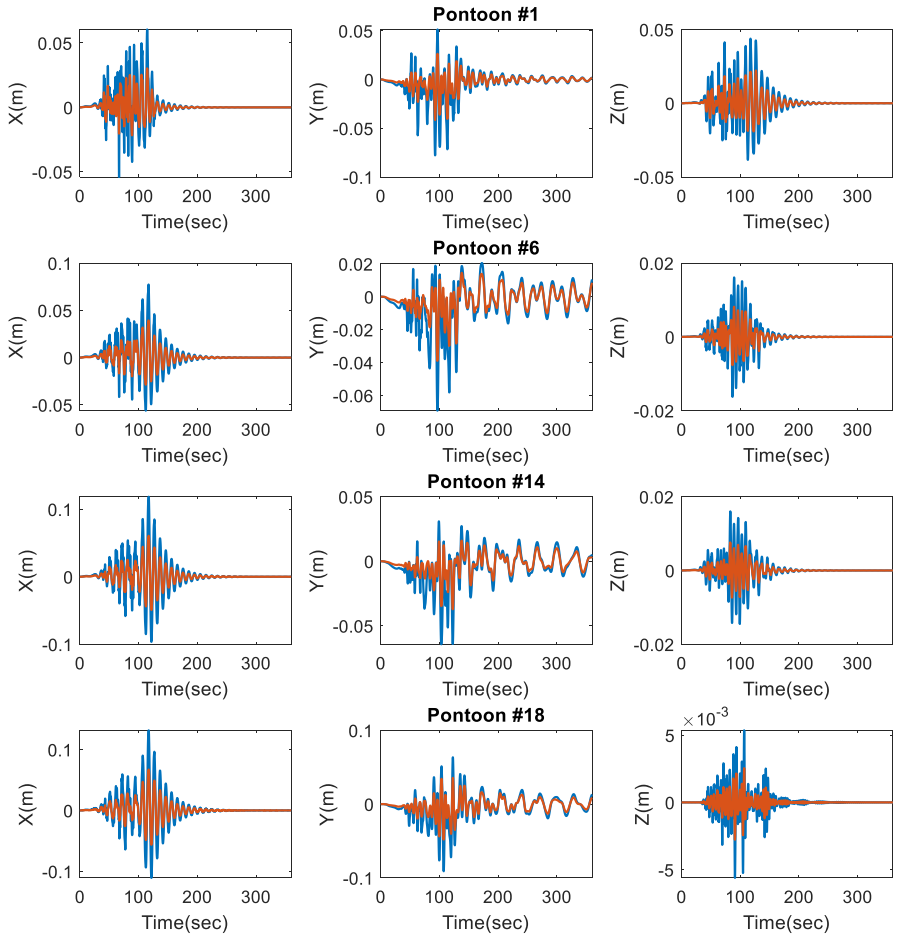

Fig. 13 3-DOF motion displacements (blue: S5 and orange: S1)

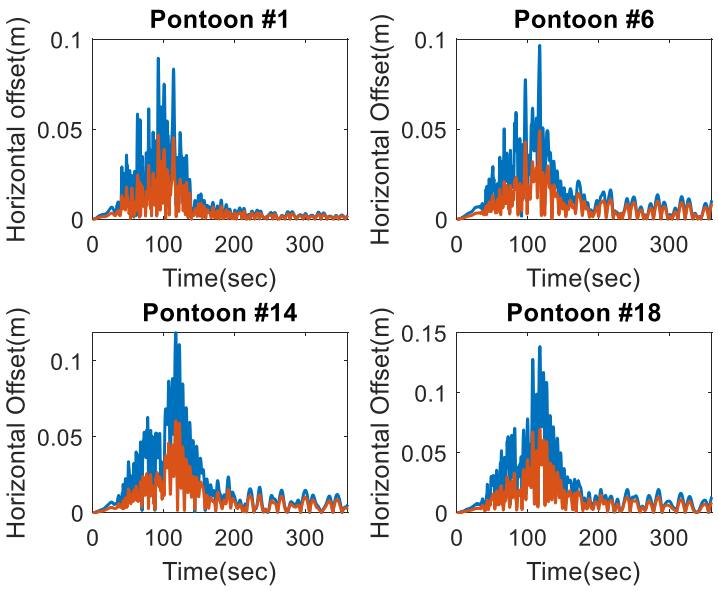

Fig. 14 Horizontal offsets for 4 pontoons (blue: S5 and orange: S1)

compare the seismic responses, we selected pontoons and mooring legs respectively at 4 different locations as shown in Figs. 2(a) and 2(b). The 3-DOF motion (XY-plane) time-series are presented in Figs. 13 and 14. According to Fig. 13, the dynamic responses for S5 are much greater than those of S1. This is because, as shown in Fig. 6, the ground motion for stiffer soils exhibits narrower spectrum with smaller energy, which results in smaller bridge-motion amplitudes. In Fig. 14, one can see that the maximum horizontal offset occurs at the center pontoon (#18) not connected to mooring lines while pontoon #6 and #14 are directly influenced by mooring lines from oscillating anchors. The horizontal offset increases as it gets close to the center of the bridge. In addition, the maximum offsets of the S1 are almost half of S5.

We next checked hydrodynamic loads acting on the selected pontoons as shown in Fig. 15. Since waves and currents are not present in the earthquake-only simulations, added mass and radiation damping forces are associated with the pontoon's seismic-induced responses. In the present numerical model, potential theory was used to solve full hydrodynamic interactions among multiple pontoons and viscous damping is not included, which can be considered through Morison equation when needed. It is interesting to see that the radiation forces are larger at pontoon #1. We observe in Figs. 13 and 14 that the pontoon's motion increases as it gets close to the middle of the bridge, but it does not ensure larger radiation forces. However, the two moored pontoons (#6 and #14) have smaller heave responses in Fig. 13. Since the left end of the bridge is oscillated by forced seismic motions, pontoon #1 shows the largest heave motion and radiation force.

Next, we present mooring fairlead tensions in Fig. 16. The line #2 and line #26 show similar mean and dynamic tensions and their mean and maxima are smaller than those of lines #10 and #18 located closer to the mid-length of the bridge. The main reason of larger maximum tensions in the mooring lines close to the mid-length of the bridge (#10 and #18) is the larger static tensions. Their dynamic tensions are also larger although identical ground motions are inputted to all anchors.

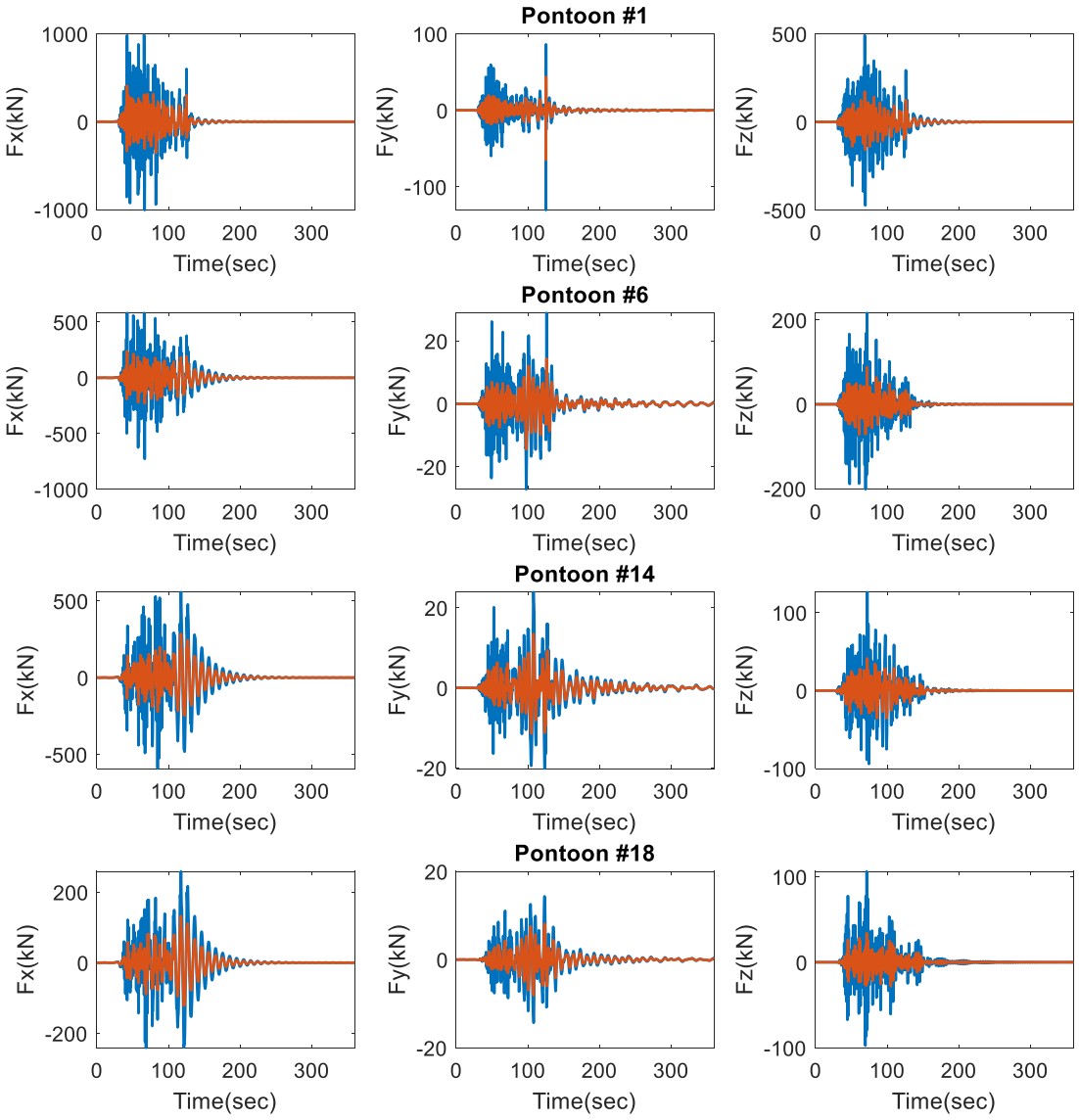

Fig. 15 Added mass + Radiation damping forces (blue: S5 and orange: S1)

We next arranged statistical values across the girders of the bridge. The mean, standard deviation, and maximum values for vertical and horizontal bending moments are presented in Figs. 17(a) and 17(b). Similar to the previous section, the mean values dominate the vertical bending moment and the differences in maxima between S1 and S5 are small. As for the horizontal bending moment in Fig. 21, S5 values are higher (more than twice) than S1 values due to larger dynamics. When motion results are compared, the standard deviation and maximum of the hard ground case (S1) are less than the half of soft-ground values (S5), as shown in XYZ-displacements Figs. 17(c)-17(e).

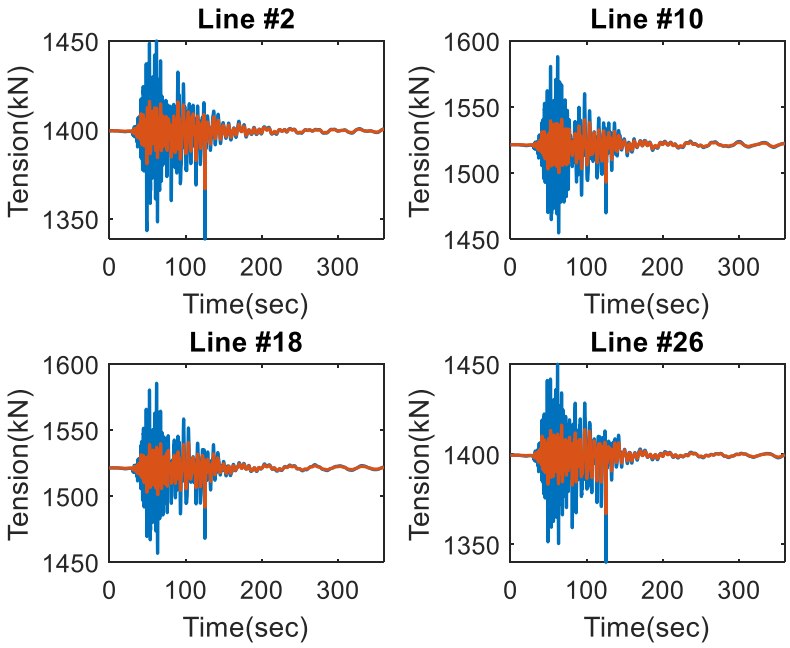

Fig. 16 Mooring tensions at 4 selected mooring legs (blue: S5 and orange: S1)

4.3 Combined earthquakes (S5 soil) + waves(1YRP)

Finally, we investigated the dynamic behavior of the floating bridge under combined waves and earthquakes. Two homogeneous wave conditions for 1YRP (year return period) and 100YRP are given in Ref. (Dai *et al*. 2020). Since it has very low probability that the design earthquake event takes place during the design wave condition (100YRP), we restrict the wave condition to be 1YRP where significant wave height is 1.3m, peak period is 4.6s, and direction of the wind-sea is 252 degrees in OrcaFlex environment setting (see Fig. 2(a)). Here, the peak enhancement factor 2.1 is determined based on the met ocean analysis report (Multiconsult 2018) which suggests 1.8-2.3 for wind sea for the site, Bjørnafjorden, and this value is very close to 2.1 for South Korea. The input JONSWAP spectrum captured from OrcaFlex is given in Fig. 18. The earthquake signal is for the deep and soft ground (S5).

The simulation time for the present study is 12 minutes with 1 minute of transient duration. Since the earthquakes last only 125 seconds, the time-domain results were illustrated up to 6 minutes for the better comparison whereas statistical values were estimated from 12 minutes data. Due to much shorter duration (about 2 minutes) of the earthquake signal compared to continuous wave signal, the standard deviation of earthquake-induced dynamics from the 12-minute signal may be appreciably underrepresented.

For comparison, following three scenarios are compared against each other.

- Earthquake only
- Wave only

Earthquake + Wave (simulataneous)

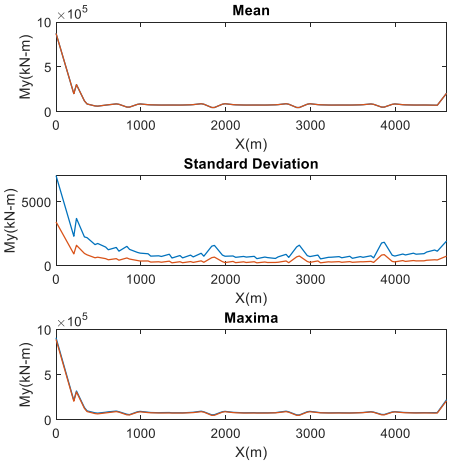

(a) Vertical bending moment

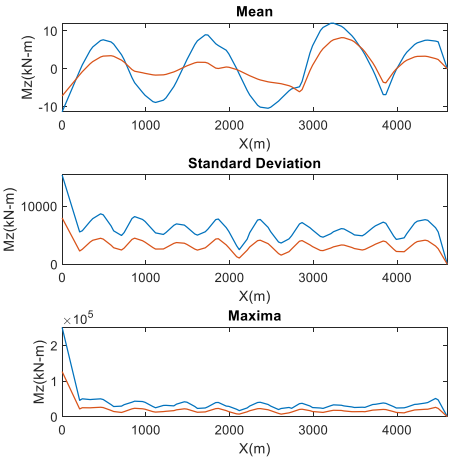

(b) Horizontal bending moment

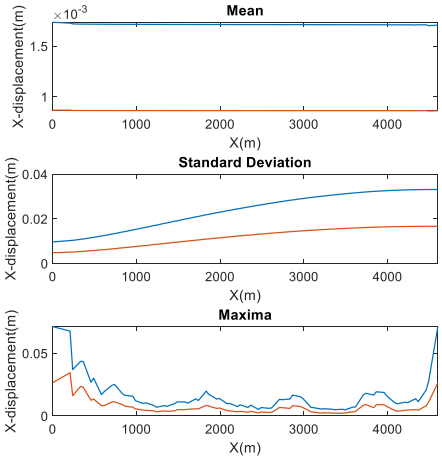

(c) girder X-displacement

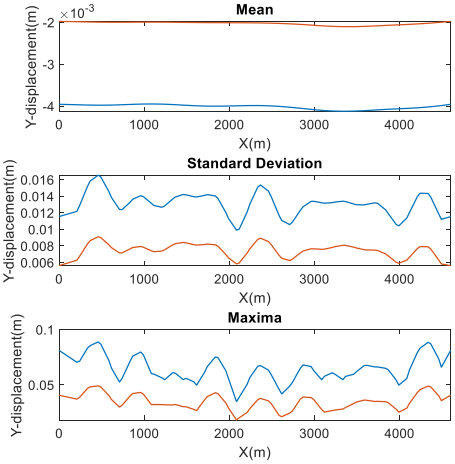

(d) girder Y-displacement

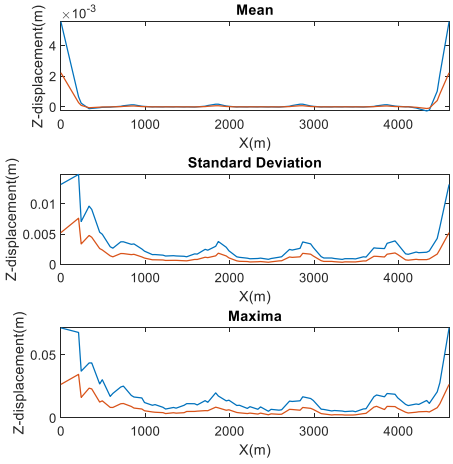

(e) girder Z-displacement

Fig. 17 Statistical values across bridge: (blue: S5 and orange: S1)

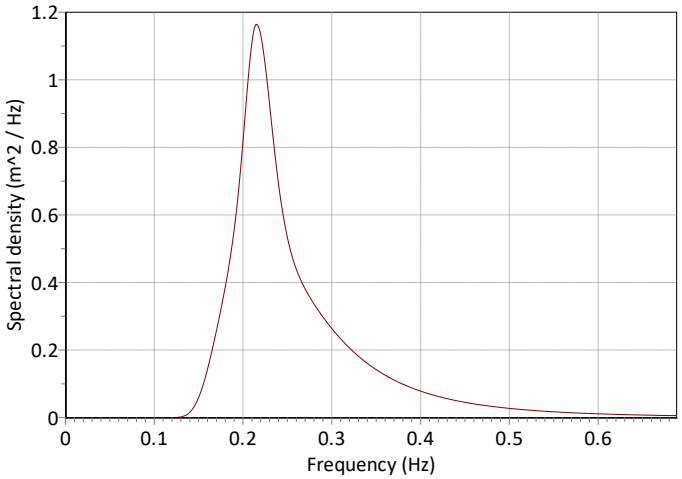

Fig. 18 JONSWAP wave energy spectrum for 1YRP (significant wave height Hs = 1.3 m, spectral peak period Tp = 4.6s, overshooting parameter γ =2.1)

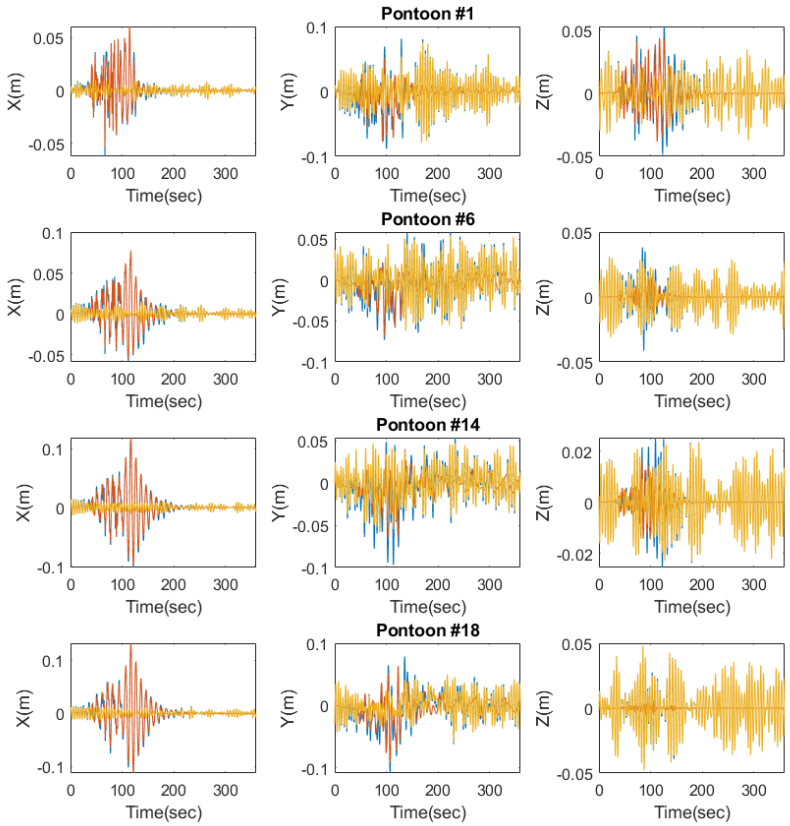

Fig. 19 3-DOF motion displacements (blue: combined, orange: earthquake only, yellow: wave only)

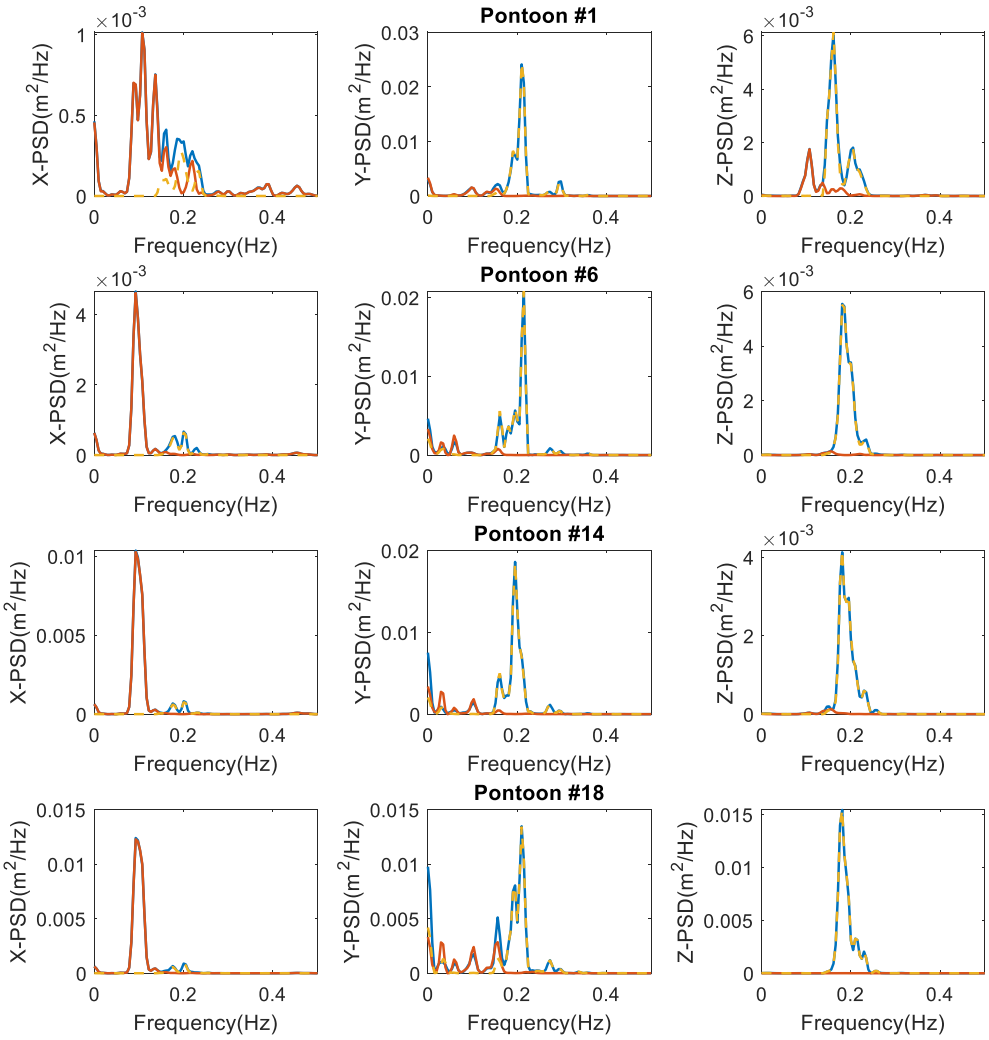

Fig. 20 Motion response spectra (blue-solid: combined, orange-solid: earthquake only, yellow-dashed: wave only)

For better comparison, the same seed of random phase is used for wave generation. First, 3-DOF motion time-series are shown in Fig. 19. It is observed that X-displacement is dominated by seismic motions whereas Y- and Z-displacements are dominated by waves. Recalling 252 degrees of incoming wave heading angle, this observation is obvious. It is very interesting to see that the largest X-displacement peak of the pontoon #18 (mid-length pontoon) in the earthquake-only simulation is greater than that of the combined earthquake and wave. It is obvious that the wave-induced and earthquake-induced responses are not in phase there to each other. In Fig. 20, the motion response spectra of the XYZ-displacements are presented. The peak frequency of the earthquake is around 0.1 Hz (pronounced in surge) while that of the waves is 0.2 Hz (pronounced in sway and heave).

In Fig. 21, horizontal offsets (XY combined) are presented for the selected pontoons. In general, the maximum offset is determined by earthquakes.

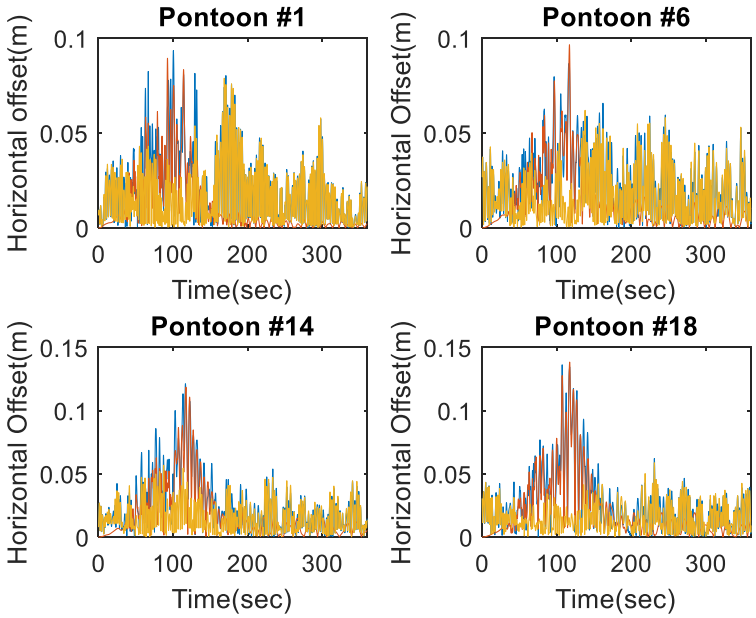

Fig. 21 Horizontal offsets for 4 pontoons (blue: combined, orange: earthquake only, yellow: wave only)

Fig. 22 shows the comparison of radiation forces (added mass + radiation damping) on selected pontoons in X-, Y-, Z-directions (See Fig. 2(a)). Aligning with the previous motion results, X-direction radiation force is dominated by earthquake signals while Y- and Z- radiation forces are dominated by waves except for the pontoon #1. However, considering their magnitudes, the radiation forces due to seismic motions are noticeably larger than those due to waves. In Fig. 23, the radiation forces are compared against the 1st-order wave diffraction forces in the combined simulation. Along Y-direction, the wave diffraction forces are larger than the radiation forces while the opposite is true in X- and Z-directions.

Figs. 24 and 25 show the time-series and power spectra of fairlead tensions at the prescribed 4 mooring lines (See Fig. 2(b)). First of all, it is observed that static tensions for mooring lines (#10 and #18) of the near center pontoons are larger. This is due to the fact that net-buoyancy loads are maintained mainly by the mooring groups there. Whereas, for outward mooring groups #2 and #26, the net buoyancy is partially supported by the constrained bridge ends. Furthermore, the dynamic response near the bridge center is greater and thus the corresponding mooring groups tend to have larger tensions. It is seen that the maximum mooring tensions occur by earthquakes. The dynamic tension by wave (only) is not that small compared to the earthquake case but the maximum tension magnitude for the combined excitation is about the same as the earthquake (only) result. Unlike the motion response spectrum, where the earthquake-induced peak occurred at 0.1 Hz, only small peaks are observed near 0.2, and 0.4Hz in the tension case. This is due to the fact that both girder level (by both ends) and anchor level move simultaneously by the same synchronous earthquakes and thus its effects on mooring tensions are expected to be small.

In Figs. 26 (a) and 26(b), the vertical and horizontal bending moment statistics across the bridge are presented. Again, the static component is dominant in the vertical bending moment. In general,

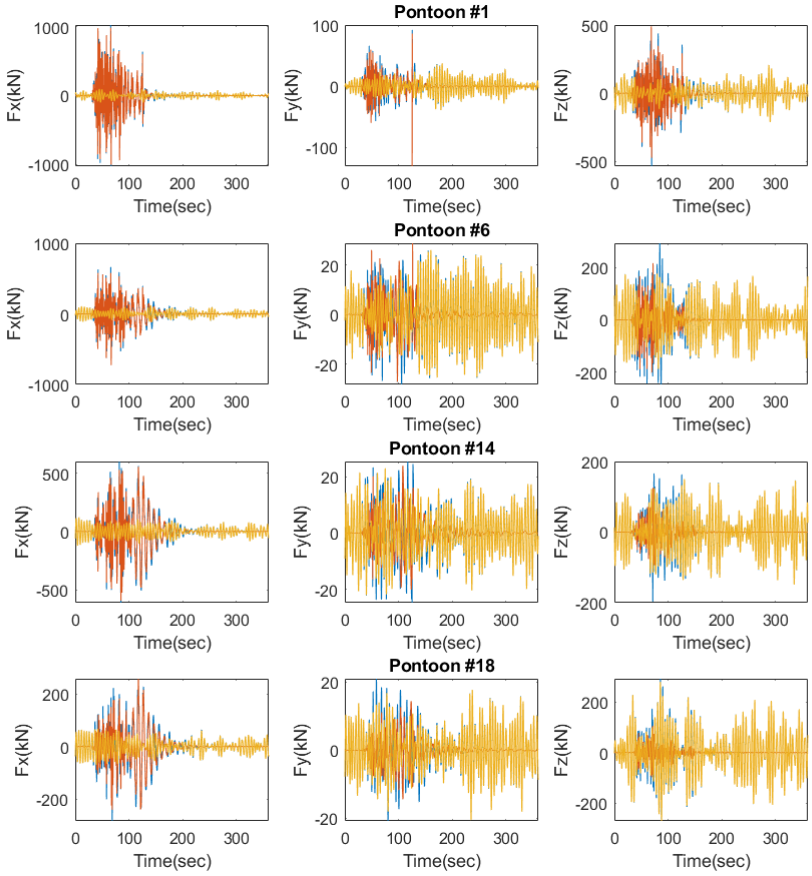

Fig. 22 Added mass + Radiation damping forces on selected pontoons (blue: combined, orange: earthquake only, yellow: wave only)

the standard deviation of the earthquake is far below that of the wave since earthquake persists in smaller time interval. As for the maximum values, there exist small discrepancies among the three scenarios except for the left end, where earthquake effects are dominant compared to wave effects. Again, the right end is free in x direction, so it should have zero horizontal bending moment there.

Figs. 26(c)-26(e) show statistical values for XYZ-displacements at girders. The maximum values are dominated by waves except for the left end in surge. In the case of Y-displacement, the maximum values by earthquake and wave are similar except for the two bridge ends. The combined results show some discrepancies from the two other results along this direction.

5. Conclusions

In this study, we investigated the effect of earthquakes on a straight floating bridge model. Ground motions for 200 YRP of South Korea were generated for two different site classes (soil conditions S1 and S5) by applying the spectral matching method to California earthquake record.

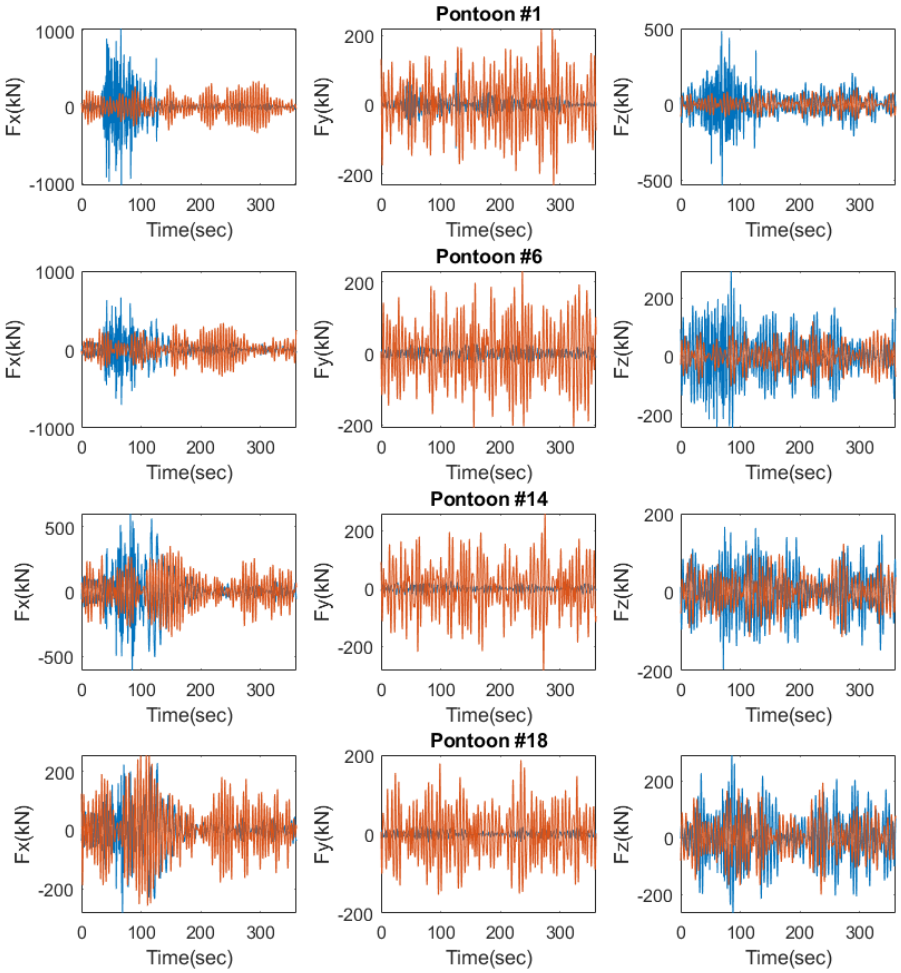

Fig. 23 Comparison of hydrodynamic forces acting on pontoons in combined earthquake + waves (blue: radiation force and orange: 1st-order wave diffraction force)

The generated ground motions were inputted to the pre-built OrcaFlex floating bridge model. A simple methodology to impose the seismic motions in the dynamic simulation program was briefly described. In order to check the impact of earthquakes, we carried out several sensitivity studies including

- Forced seismic motions for anchors only and including two ends of the bridge.
- Soil sensitivity between hard rock (S1) and deep and soft ground (S5)
- Earthquake (only) vs Wave (only) vs Combined earthquake and wave

The numerical results exhibit that the impact of earthquakes is significant. Its dynamic effects, horizontal offsets, and horizontal bending moments are generally larger in soft soil (S5) than hard soil (S1). Indeed, the pontoon's maximum offset, which is a key design consideration of floating structures, is dominated by the earthquake signals. The X-direction girder response is particularly susceptible to the earthquake and increases toward the middle of the bridge. When the earthquake

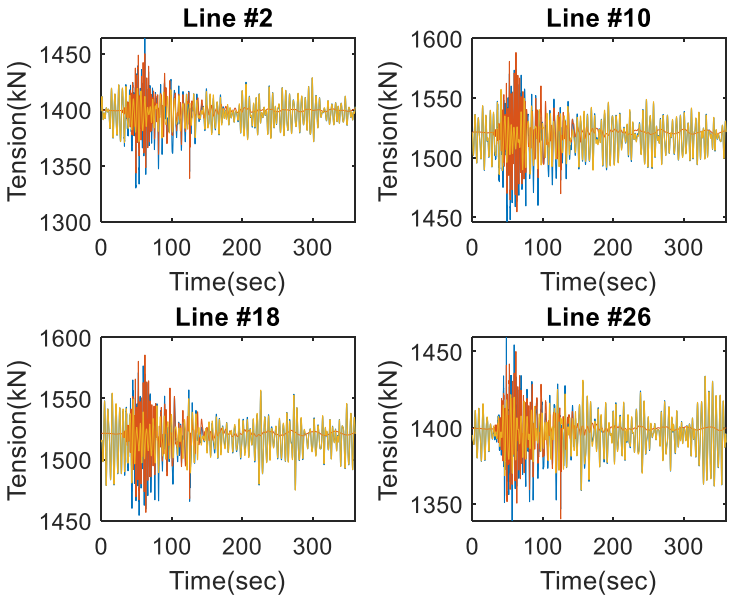

Fig. 24 Mooring tensions at 4 selected mooring legs (blue: combined, orange: earthquake only, yellow: wave only)

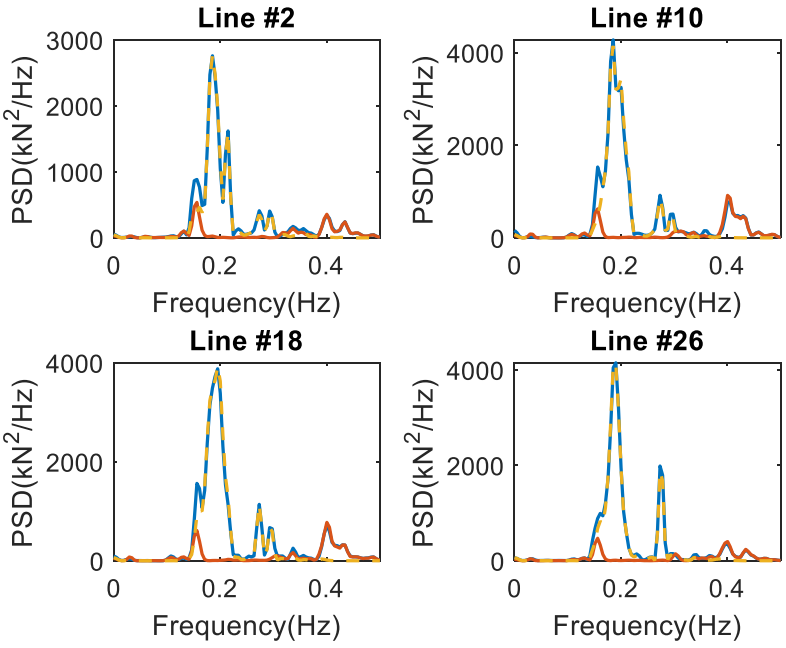

Fig. 25 Mooring tension power spectrum for 4 selected mooring legs (blue-solid: combined, orange-solid: earthquake only, yellow-dashed: wave only)

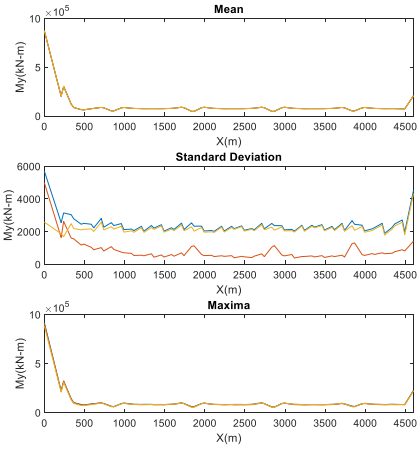

(a) Vertical bending moment

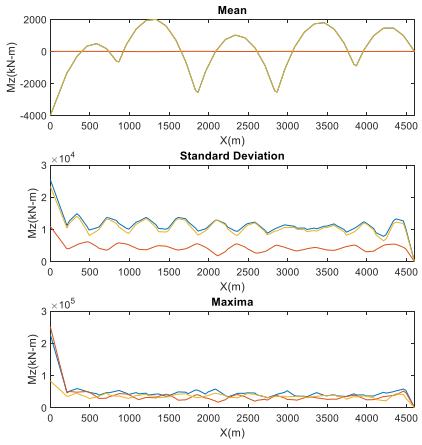

(b) Horizontal bending moment

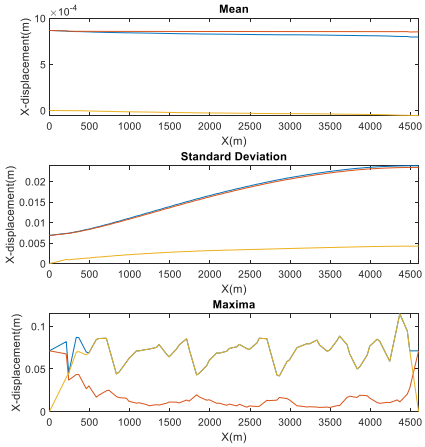

(c) girder X-displacement

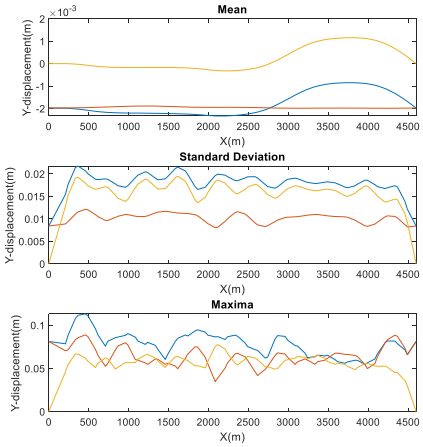

(d) girder Y-displacement

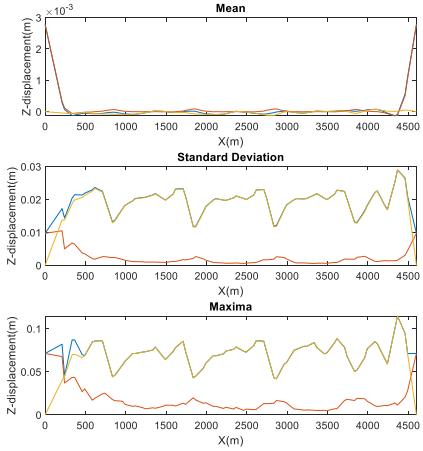

(e) girder Z-displacement

Fig. 26 Statistical values across bridge: (blue: combined, orange: earthquake only, yellow: wave only)

coexists with 1YRP wave, the maximum vertical bending moment is governed by the static component and the maximum horizontal bending moment is dominated by earthquake excitation. The effects of earthquake on mooring lines are alleviated since girder level (at both ends) and anchor level move simultaneously in a synchronous manner. The maximum mooring tensions near the center are larger than those near the ends. The impact of earthquakes on floating bridges is still of importance especially for soft soil although ground motions are less directly applied to the structure than fixed bridges.

In the present study, we neglected seaquake effect which is caused mostly by vertical ground motion of the seabed. Considering that the pontoon is floating and located 300m above the seabed, its influence can be assumed negligible (Jin and Kim 2018). Although we only considered the bridge response for a single homogeneous and fully correlated earthquake, numerous types of different design load cases can be developed according to the presence of swell, current, and wind with specified guidelines for ULS, FLS and ALS analysis.

As future works associated with the earthquake analysis of floating bridges, the authors suggest:

- Different choices of boundary conditions at the bridge ends considering real structure end connections. (It has been assumed in the present study that surge and yaw DOFs are allowed to move freely at the right end.).
- Seismic wave effect can be implemented by giving different magnitudes and phases for individual anchor and bridge ends considering the seismic wave propagation speed, direction, and soil types.

Acknowledgments

This work was supported by a Korea Agency for Infrastructure Technology Advancement (KAIA) grant funded by the Ministry of Land, Infrastructure, and Transport (Grant RS-2023-00250727) through the Korea Floating Infrastructure Research Center at Seoul National University.

References

Al Atik, L. and Abrahamson, N. (2010), "An improved method for nonstationary spectral matching", *Earthq. Spectra*, **26**(3), 601-617. https://doi.org/10.1193/1.34591.

Cheng, Z., Gao, Z. and Moan, T. (2018a), "Hydrodynamic load modeling and analysis of a floating bridge in homogeneous wave conditions", *Mar. Struct.*, **59**, 122-141. https://doi.org/10.1016/j.marstruc.2018.01.007.

Cheng, Z., Gao, Z. and Moan, T. (2018b), "Wave load effect analysis of a floating bridge in a fjord considering inhomogeneous wave conditions", *Eng. Struct.*, **163**, 197-214. https://doi.org/10.1016/j.engstruct.2018.02.066.

Cheng, Z., Gao, Z. and Moan, T. (2019), "Numerical modeling and dynamic analysis of a floating bridge subjected to wind, wave, and current loads", *J. Offshore Mech. Arct. Eng.*, **141**, 011601. https://doi.org/10.1115/1.4040561.

Cheng, Z., Gao, Z. and Moan, T. (2020), "Extreme responses and associated uncertainties for a long end-anchored floating bridge", *Eng. Struct.*, **219**, 110858. https://doi.org/10.1016/j.engstruct.2020.110858.

Dai, J., Leira, B.J., Moan, T. and Kvittem, M.I. (2020), "Inhomogeneous wave load effects on a long, straight and side-anchored floating pontoon bridge", *Mar. Struct.*, **72**, 102763. https://doi.org/10.1016/j.marstruc.2020.102763.

Jang, M., Lee. Y., Won, D., Kang, Y.J. and Kim, S. (2020a), "Static behaviors of a long-span cable-stayed bridge with a floating tower under dead loads", *J. Mar. Sci. Eng.*, **8**(10), 816. https://doi.org/10.3390/jmse8100816.

Jang, M., Lee, Y., Kim, S. and Kang, Y.J. (2020b), "Dynamic behavior of a long-span cable-stayed bridge with floating towers after the sudden failure of tethers and cables under irregular waves", *J. Mar. Sci. Technol.*, **28**(6), 593-601. https://doi.org/10.6119/JMST.202012_28(6).0014.

Jin, C. and Kim, M.H. (2018), "Time-domain hydro-elastic analysis of a SFT (submerged floating tunnel) with mooring lines under extreme wave and seismic excitations", *Appl. Sci.*, **8**(12), 2386. https://doi.org/10.3390/app8122386.

Jin, C., Kim, M., Chung, W.C. and Kwon, D.S. (2020), "Time-domain coupled analysis of curved floating bridge under wind and wave excitations", *Ocean Syst. Eng.*, **10**(4), 399-414. https://doi.org/10.12989/ose.2020.10.4.399.

Jin, C., Kim, S., Chung, W.C., Kang, B. and Kim, S. (2024), "Feasibility investigation of tuned mass damper for vibration control of curved floating bridge in winds and waves", *Appl. Ocean Res.*, **148**, 104013. https://doi.org/10.1016/j.apor.2024.104013.

Multiconsult (2017), SBJ-31-C3-MUL-22-RE-100-0 – analysis and design (base case). Oslo, Norway: Multiconsult AS.

Multiconsult (2018), SBJ-01-C4-SVV-01-BA-001 – MetOcean Design basis. Oslo, Norway: Multiconsult AS.

Orcina (2024), *OrcaFlex Manual* (https://www.orcina.com/webhelp/OrcaFlex/).

Rodrigues, J.M., Viuff, T. and Ø kland, O.D. (2022), "Model tests of a hydroelastic truncated floating bridge", *Appl. Ocean Res.*, **125**, 103247. https://doi.org/10.1016/j.apor.2022.103247.

Viuff, T., Xiang, X., Leira, B.J. and Øiseth, O. (2020a), "Software-to-software comparison of end-anchored floating bridge global analysis", *J. Bridge Eng.*, **25**(5), 04020022. https://doi.org/10.1061/(ASCE)BE.1943-5592.0001545.

Viuff, T., Xiang, X., Ø iseth, O. and Leira, B.J. (2020b), "Model uncertainty assessment for wave- and current-induced global response of a curved floating pontoon bridge", *Appl. Ocean Res.*, **105**, 102368. https://doi.org/10.1016/j.apor.2020.102368.

Viuff, T., Ravinthrakumar, S., Ø kland, O.D., Gryta, O.A. and Xiang, X. (2023), "Model test of a hydroelastic truncated floating bridge with a stay-cable tower", *Appl. Ocean Res.*, **135**, 103539. https://doi.org/10.1016/j.apor.2023.103539.

Won, D., Lee, K., Kang, Y.J. and Kim, S. (2020), "Short-term fatigue damage of tethers of long-span floating cable supported bridges under harsh waves", *J. Mar. Sci. Technol.*, **28**(6), 602-609. https://doi.org/10.6119/JMST.202012_28(6).0015.

Xiang, S., Cheng, B., Li, D., Tang, M. and Zeng, Z. (2023), "Structural dynamic performance of floating continuous beam bridge under wave and current loadings: An experimental study", *Appl. Ocean Res.*, **137**, 103604. https://doi.org/10.1016/j.apor.2023.103604.

Yadi, S., Suhendro, B., Priyosulistyo, H. and Aminullah, A. (2018), "Shake table test of floating cable-stayed bridge under earthquake excitation during construction with balanced cantilever method", *Int. J. Civ. Eng. Technol.*, **9**, 2063-2081.

Yan, J., Liu, J., Liu, Z., Li, H. and Guo, A. (2023), "Experimental study on the dynamic responses of the end-anchored floating bridge subjected to joint actions of earthquakes and water waves", *Earthq. Eng. Struct. D.*, **52**(10), 2945-2965. https://doi.org/10.1002/eqe.3904.

Yan, J., Liu, J., Liu, Z. and Guo, A. (2024a), "Experimental study on the effects of hydrodynamic loads on the seismic response of end-anchored floating bridges", *Ocean Eng.*, **300**, 117464. https://doi.org/10.1016/j.oceaneng.2024.117464.

Yan, J., Liu, J., Liu, Z. and Guo, A. (2024b), "Time domain simulation of a floating bridge subject to the joint actions of an earthquake and wave actions", *Ocean Eng.*, **295**, 116992. https://doi.org/10.1016/j.oceaneng.2024.116992.